Nanoscale

PAPER

View Article Online
View Journal | View Issue

Cite this: *Nanoscale*, 2025, **17**, 10677

Nanostructured films from poly(3-hexylthiophene)-*graft*-poly(ε-caprolactone) as light-responsive generators of reactive oxygen species†

Ilaria Abdel Aziz, [a] Elena Gabirondo, [a] Araceli Flores, [b] Pilar Posadas, [b] Haritz Sardon, [a] David Mecerreyes [a,c] and Miryam Criado-Gonzalez *[a,b]

The design of smart photoelectrodes is used to modulate and control the spatio-temporal production of reactive oxygen species (ROS). In this work, we develop photoactive films with tunable nanostructured morphologies to favor ROS production *via* photostimulation. To that aim, we synthesized graft copolymers, made of poly(3-hexylthiophene) (P3HT) and poly(ε-caprolactone) (PCL), P3HT-*g*-PCL, which were employed to fabricate compact films by drop casting. The films were further subjected to a thermo-oxidative treatment in the presence of H_2O_2 at 42 °C. This led to nanostructured films with a porosity (~500 nm diameter and ~70 nm height) controlled at specific copolymer compositions, as determined by atomic force microscopy (AFM). The nanostructured P3HT films possess higher storage moduli (*E*′) than flat P3HT films, as determined by nanoindentation measurements. Finally, the performance of nanostructured P3HT films as photoelectrodes is assessed in a three-electrode electrochemical cell upon visible-light irradiation (λ = 467 nm), leading to the spatiotemporal production of H_2O_2 at non-cytotoxic levels for future non-invasive redox medicine applications.

Received 3rd January 2025,
Accepted 26th March 2025

DOI: 10.1039/d5nr00027k

rsc.li/nanoscale

1. Introduction

Reactive oxygen species (ROS) are biologically relevant oxidants (*i.e.*, superoxide anions, hydroxyl radicals, and the more stable hydrogen peroxide, among others) of great interest for redox medicine.[1,2] They can act as powerful cell signalling agents depending on their concentration.[3] When overproduced, ROS can induce harmful effects on cell viability, causing cell apoptosis, inflammation, cardiovascular diseases, and even cancer.[4] Otherwise, the production of ROS at non-cytotoxic concentrations can be highly beneficial in most biological processes (*i.e.*, differentiation, proliferation, and migration) as they finely regulate both eustress and distress conditions to target physiological conditions.[5] ROS are produced endogenously in the plasma membrane, although this process is irreversible and presents limited spatiotemporal resolution.[6,7] This drawback can be overcome through the exogenous production of ROS by physical stimulation (*i.e.*, light, voltage, or acoustic waves) of functional materials.[8,9] In particular, the use of light is gaining increasing attention as it provides wireless stimulation, low invasiveness, reversibility, and high spatial selectivity.[10] Indeed, the development of smart photoactive materials that can finely tune the ROS concentration at safe power densities during photostimulation is actively being pursued. Semiconducting polymers (SPs) have attracted increasing interest in biophotonics due to their intrinsic optical properties, conductivity, chemical versatility, biocompatibility, and soft nature.[11] In particular, they show optical absorption properties in the visible or near-infrared region, making them appealing for bioelectronics applications, as such wavelengths are not harmful (compared to UV light for example) and can penetrate superficial skin layers.[12] All these features make them ideal candidates to control localized photoelectrochemical reactions and accomplish the multifunctional properties required for tissue–material interfaces.[13,14] Among different SPs, poly(3-hexylthiophene) (P3HT) is a p-type polymer known for its remarkable optoelectronic properties. It has been used as a photocathode in an aqueous environment under aerobic conditions, generating H_2O_2 and other intermediate ROS on the semiconductor surface.[15–18] P3HT-based nanomaterials have demonstrated excellent ability to interact with living cells and generate ROS upon

[a]*POLYMAT, University of the Basque Country UPV/EHU, Joxe Mari Korta Center, Avda. Tolosa 72, 20018 Donostia-San Sebastián, Spain*
[b]*Institute of Polymer Science and Technology (ICTP-CSIC), 28006 Madrid, Spain. E-mail: mcriado@ictp.csic.es*
[c]*Ikerbasque, Basque Foundation for Science, 48013 Bilbao, Spain*

† Electronic supplementary information (ESI) available: Phase and topographical AFM images of the P3HT and P3HT-*g*-PCL films; optical microscopy images of the P3HT-*g*-PCL films; nanoindentation measurements of the P3HT-*g*-PCL films; photocurrent measurements; and H_2O_2 production measurements. See DOI: https://doi.org/10.1039/d5nr00027k

visible light irradiation to trigger intracellular calcium ion flux or induce redox signaling processes. It is noteworthy that the performance of P3HT-based materials is greatly influenced by their morphological properties at the nanoscale when processed in the form of thin films and nanoparticles.[19–21] For topical applications, the development of innovative smart nanostructured films is desired, for use as photoactive dermal patches for minimally invasive photostimulation therapies. Very recently, P3HT-*graft*-poly(L-lactic acid) (PLA) copolymers were used to fabricate nanoporous thin films through the alkaline hydrolysis (1 M NaOH) of PLA segments. These nanoporous P3HT thin films showed enhanced photofaradaic behavior, generating a higher concentration of ROS compared to non-porous P3HT films for extracellular photostimulation of endothelial cells.[17,22,23] Herein, we investigate a different approach to generate nanostructured and nanoporous P3HT films by a thermo-oxidative process that mimics pathophysiological inflammatory diseases (*i.e.*, high production of ROS and febrile states). For such a purpose, P3HT-derived graft copolymers were synthesized by the macromonomer method using poly(ε-caprolactone) (PCL) as a polyester macromonomer. The effect of the copolymer molecular composition on the thermo-oxidative process, the pore size, and the nanostructured morphology of the films were studied. Finally, the nanostructured films were tested as photoelectrodes to optically modulate the ROS production, at non-cytotoxic concentrations and in a wireless manner under visible light irradiation.

2. Results and discussion

Graft copolymers combining poly(3-hexylthiophene) (P3HT) and poly(ε-caprolactone) (PCL), P3HT-*g*-PCL, were synthesized by the macromonomer method (Scheme 1). PCL was chosen due to its lower glass transition ($T_g \geq -60$ °C) and melting ($T_m > 60$ °C) temperatures, which give flexibility and biocompatibility for constructing copolymers as previously reported for electroactive poly(3,4-ethylenedioxythiophene) (PEDOT) graft copolymers (PEDOT-*g*-PCL).[24] In the first step, an α-EDOT-PCL macromonomer was synthesized by ring-opening polymerization (ROP) of ε-caprolactone, following a previously reported protocol.[24] EDOT-methanol was used as a chain initiator and a mixture of methanesulfonic acid (MSA) and 4-dimethylaminopyridine (DMAP) in a ratio of 1 : 1 was used as an organocatalyst. The molecular weight of the EDOT-PCL macromonomer, 9700 g mol^{-1}, was determined through the relative intensities of the ^{1}H-NMR signals corresponding to the thiophene protons at 6.4 ppm and the –CH_2– aliphatic polyester chain at 4.3 ppm (Fig. 1). In a second step, P3HT-*g*-PCL graft copolymers were synthesized by chemical oxidative polymerization of the α-EDOT-PCL macromonomer and 3-hexylthiophene (3HT) using $FeCl_3$ as an oxidant in a molar ratio of 4 : 1 of $FeCl_3$: 3HT. P3HT$_x$-*g*-PCL$_y$ graft copolymers with different P3HT (x) and PCL (y) molar percentages were obtained by changing the feed ratio of 3HT : PCL in the reaction. Yields higher than 40% were obtained in all cases, and the proportions of the two components in the graft copolymers were determined by ^{1}H NMR (Fig. 1). The spectra showed the characteristic signals of the hydrogen of the methylene unit near the ester group of PCL at 4.1 ppm[25] and the –CH_3– of P3HT at 0.9 ppm.[26] The final molar composition of each component in the graft copolymers was determined through the ratio between the integrated signals of P3HT and PCL, leading to two different copolymers: P3HT$_{95}$-*g*-PCL$_5$ and P3HT$_{85}$-*g*-PCL$_{15}$.

Next, the synthesized copolymers were dissolved in a mixture of chlorobenzene and chloroform (1 : 1%v/v) at 70 °C and dropcasted on top of indium–tin–oxide (ITO)-glass substrates to obtain compact films (Fig. 2A and Table S1†). The morphology of the films was characterized by atomic force microscopy (AFM), as shown in Fig. 2B. P3HT$_{95}$-*g*-PCL$_5$ films exhibited a surface topography with round domains that could be attributed to the micro-phase separation of PCL, as such domains were not displayed in P3HT films used as a control (Fig. S1†). It is known that micro-phase separation in copoly-

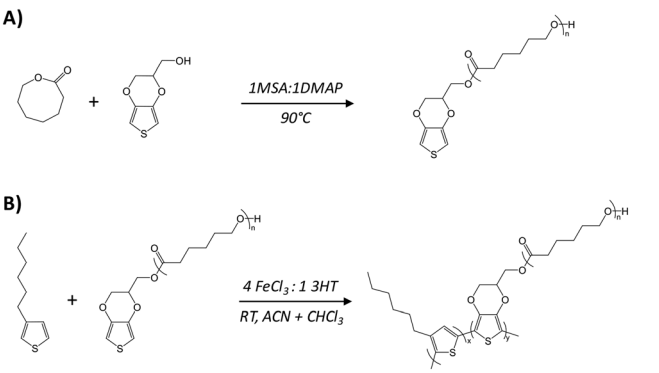

Scheme 1 Chemical routes employed to synthesize: (A) the α-EDOT-PCL macromonomer by ROP and (B) P3HT-*g*-PCL copolymers by chemical oxidative polymerization.

Miryam Criado-Gonzalez

Dr Miryam Criado-Gonzalez is a Ramón y Cajal Assistant Researcher at the Institute of Polymer Science and Technology (CSIC), Spain. She leads a research team studying smart polymeric and polypeptide materials for biomedical applications. Her research interests include the synthesis of bio-based functional polymers and polypeptides and the study of their self-assembly, as well as the development of intelligent nanomaterials and gels and their additive manufacturing processes through 3D/4D printing technologies for advanced applications in the biomedical field. She received the Young Researcher Award from the European Materials Research Society (E-MRS) in 2021 and the Emakiker researcher position at POLYMAT in 2022.

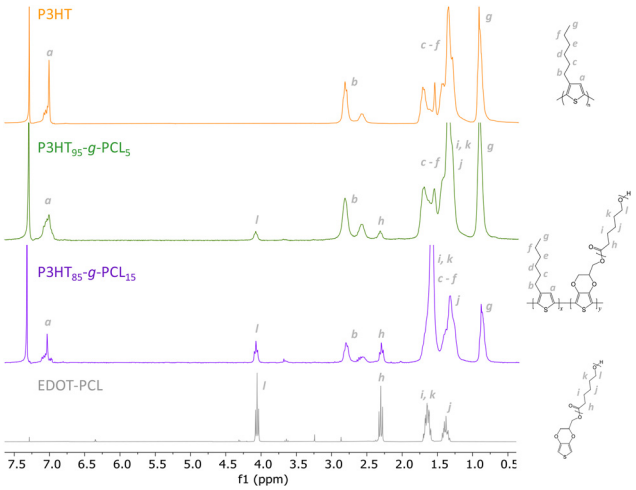

Fig. 1 ^{1}H NMR spectra of the synthesized macromonomer α-EDOT-PCL, the homopolymer P3HT, and the graft copolymer P3HT$_x$-*g*-PCL$_y$.

mers is influenced by different aspects such as composition, copolymer architecture, or crystallinity. This is even more evident in the case of graft copolymers, where one of the polymer blocks is composed of a conducting or semiconducting polymer.[22,27,28] On the other hand, films prepared with the copolymer P3HT$_{85}$-*g*-PCL$_{15}$ showed a homogeneous surface similar to those prepared with the homopolymer P3HT. In all cases, the films presented very low surface roughness ($R_a \leq$ 1.0 nm). Then, we exposed the films to extreme thermo-oxidative conditions, which are present in inflammatory areas in the human body that are characterized by a high production of ROS (*i.e.*, H_2O_2) and febrile conditions. For such a purpose, the films were immersed in an aqueous solution of 100 mM H_2O_2 at 42 °C for 48 h. The films prepared from the graft copolymer P3HT$_{95}$-*g*-PCL$_5$ showed substantial changes, with the appearance of pores, evident as round dark areas in the AFM micrographs (Fig. 2C) and an increase of the surface roughness ($R_a \approx$ 5.7 nm). The dimensions of the pores (~500 nm diameter and ~70 nm height) were determined by surface height profiles in the representative areas of the micrographs (Fig. 2D and Fig. S2†). This could be attributed to the partial degradation of α-EDOT-PCL segments in the presence of H_2O_2, resulting in mixtures of the EDOT-derived sulfone (*via* sulfoxide intermediate) and the thiolactone heterocycle 3,4-ethylenedioxy-2(5H)thiophenone,[29,30] together with the possible oxidation of the sulfur atom present in the thiophene ring of P3HT, leading to mixtures of sulfoxide (thienyl-1-oxide) and sulfone (thienyl-1,1-dioxide),[31,32] as demonstrated by changes in the signal of the thiophene protons at 7.0 and 6.5 ppm in the ^{1}H-NMR spectra (Fig. S3†). In contrast, in the case of

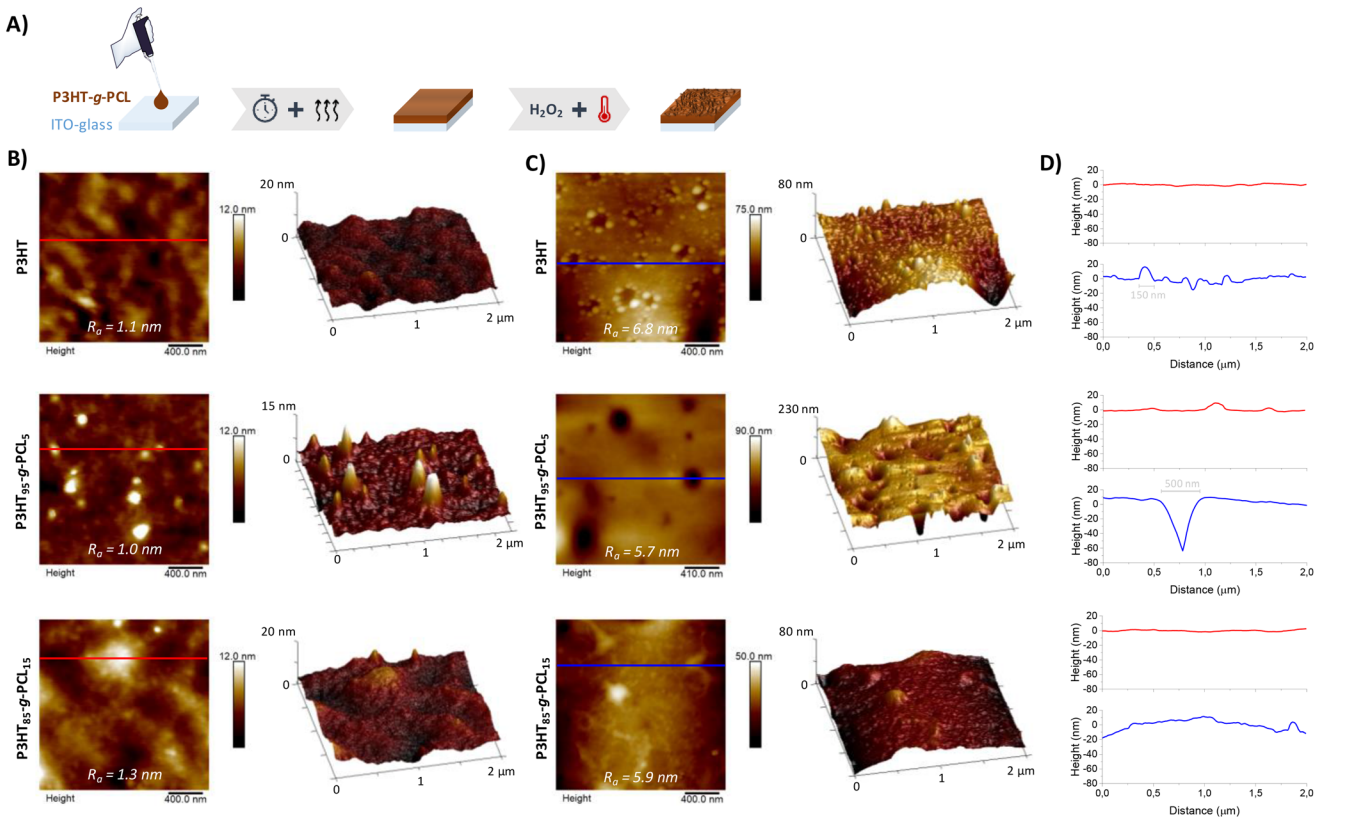

Fig. 2 (A) Schematic representation of the fabrication of the films, followed by a thermo-oxidative step. (B) 2D (left) and 3D (right) topographical AFM images of the thin films before thermo-oxidation. (C) 2D (left) and 3D (right) topographical AFM images of the thin films after thermo-oxidation. Red and blue lines show the cut-positions to determine the pore dimensions in (D).

P3HT$_{85}$-*g*-PCL$_{15}$ films, no pores were detected in the surface height profiles of AFM images, probably because of the more homogeneous distribution of both polymers without presenting a phase separation. Surprisingly, the surface morphology of pure P3HT films also showed changes with the appearance of potholes (~150 nm diameter and ~10 nm height) and the increase of $R_a \approx 6.8$ nm. This could be due to the partial oxidation of the thioether group present in the thiophene ring of P3HT.[31,33]

Nanoindentation measurements were conducted to determine the mechanical properties of the films. In all cases, the storage modulus (E') of the films was stabilized at 150 nm penetration (Fig. 3A). In the case of P3HT films, E' reached values of 542 ± 18 MPa, whereas it decreased to $E' = 258 \pm 12$ MPa for P3HT$_{95}$-*g*-PCL$_5$ films due to the presence of more elastic PCL domains within the copolymer. In alignment with these results, the hardness (H) of the films also decreased in the copolymers, from $H = 8.7 \pm 0.4$ MPa for P3HT films to $H = 2.7 \pm 0.3$ MPs for P3HT$_{85}$-*g*-PCL$_{15}$ films (Fig. 3C). On the other hand, while P3HT$_{85}$-*g*-PCL$_{15}$ films did not show any structural changes at the nanoscale, they exhibited macrostructural aggregates (Fig. S4†), which made it difficult to perform the nanoindentation measurements. After thermo-oxidation, the storage modulus and hardness of the P3HT films increased to $E' = 676 \pm 64$ MPa (Fig. 3B) and $H = 11 \pm 1$ MPa (Fig. 3D), respectively. Similar findings were obtained for P3HT$_{95}$-*g*-PCL$_5$ films with higher $E' = 334 \pm 30$ MPa and $H = 3.4 \pm 0.3$ MPa after thermo-oxidation. This can be attributed to the nanostructural changes in the morphology of the films, as reported by other authors for other polymer systems,[34] and to the recrystallization of the amorphous polymeric chains resulting in an increased chain molecular alignment.[35,36]

P3HT$_{95}$-*g*-PCL$_5$ and P3HT$_{85}$-*g*-PCL$_{15}$ films were further characterized by measuring the (photo)electrochemical properties (Fig. 4A and Fig. S5†). In a three-electrode electrochemical cell (Fig. 4B), an ITO-glass substrate coated with the copolymer films was used as the working electrode (WE), a Pt bundle was used as the counter electrode (CE), and Ag/AgCl was used as the reference electrode (RE). All the electrodes were immersed in phosphate buffer solution (PBS), used as the electrolyte. Cyclic voltammetry (CV) recorded for both copolymers in the pristine state showed that P3HT$_{85}$-*g*-PCL$_{15}$ had a higher current and capacitive component compared to P3HT$_{95}$-*g*-PCL$_5$ (Fig. S6†), possibly indicating a higher surface area. Moreover, the former showed a higher electrocatalytic activity compared to the latter, as a higher current density is recorded for the corresponding negative potential. Upon irradiation with a blue LED (λ = 467 nm), a photocathodic behavior was recorded with an increase in current for increasing irradiation intensity for both copolymers (Fig. 4C and D). The photocathodic behavior of P3HT is ascribed to oxygen reduction reactions, as photogenerated electrons from the polymer reduce the amount of available species in the electrolyte, *i.e.*, molecular oxygen.[17,18] For P3HT$_{95}$-*g*-PCL$_5$ films, no remarkable changes were recorded in the photocurrent properties after the exposure to thermo-oxidative conditions, possibly indicating that the polymer is not strongly affected. On the other hand, for P3HT$_{85}$-*g*-PCL$_{15}$ films, an increase in the photocurrent density was observed in comparison with the non-oxidized films. We also studied the long-term stability of the films by measuring their photocurrent density during different photoexcitation cycles, using a light intensity of 67 mW cm^{-2}. All oxidized films showed good reproducibility of the photocurrent density during the different cycles with a slight loss of photocurrent generation after 5 cycles (Fig. S7†). As noted in previous studies on P3HT films and nanoparticles, the metastable photogenerated O_2^- undergoes rapid dismutation in aqueous media, leading to the formation of H_2O_2. Hence, we quantify the production of H_2O_2 in an electrochemical setup formed by a black platinum working electrode, which possesses higher sensitivity and selectivity towards H_2O_2,[37–39] Pt as the CE, Ag/AgCl as the RE, and PBS as the electrolyte (Fig. 4E). H_2O_2 generation was recorded over time with the same light intensities as used for the photocurrent recordings, namely 67, 131, 205, and 255 mW cm^{-2}. The time dynamics (Fig. S8†) showed an increase in the concentration of H_2O_2 synchronous with the photostimulation. In agreement with the photocathodic behavior, an increasing H_2O_2 concentration was recorded with increasing the light intensity. Pristine P3HT$_{95}$-*g*-PCL$_5$ films gave rise to H_2O_2 concentrations at the end of the photostimulation that ranged from ~1.2 × 10^{-6} μM at 67 mW cm^{-2} up to ~1.1 × 10^{-5} μM at 255 mW cm^{-2} (Fig. 4F). Compared to pristine P3HT$_{85}$-*g*-PCL$_{15}$, P3HT$_{95}$-*g*-PCL$_{15}$ showed a higher H_2O_2 production, possibly due to a higher P3HT content. The H_2O_2 production slightly increased for porous P3HT$_{95}$-*g*-PCL$_5$ films compared to the corres-

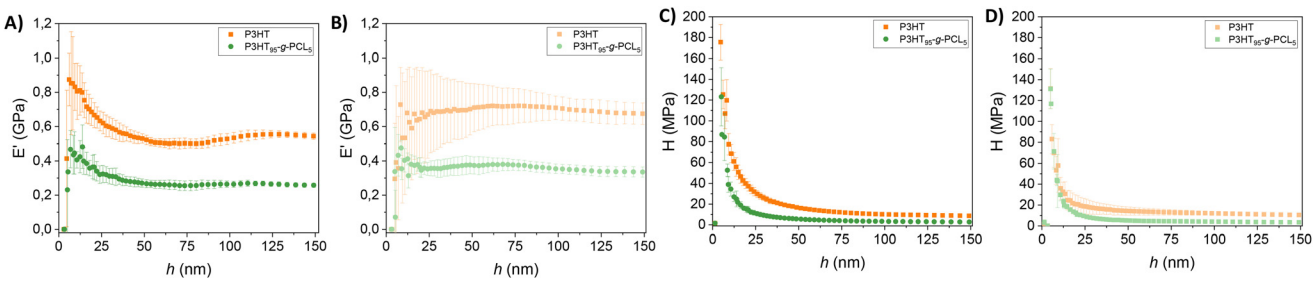

Fig. 3 Storage modulus (E') of the P3HT and P3HT$_{95}$-*g*-PCL$_5$ films (A) before and (B) after the thermo-oxidative process. Hardness (H) of the P3HT and P3HT$_{95}$-*g*-PCL$_5$ films (C) before and (D) after the thermo-oxidative process.

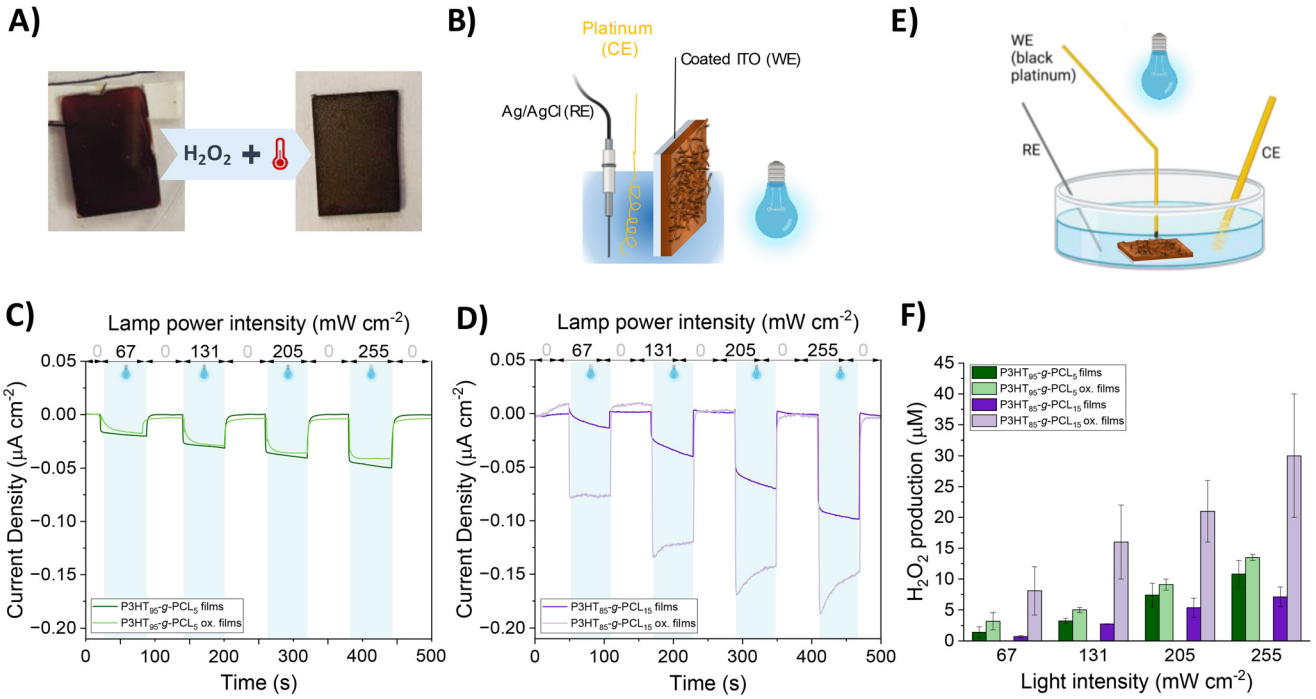

Fig. 4 (A) Images of the P3HT$_{95}$-*g*-PCL$_5$ films before and after the thermo-oxidative treatment. (B) Schematic representation of the photoelectrochemical cell (PEC) used for measuring the photocurrent properties. Photocurrent density of the (C) P3HT$_{95}$-*g*-PCL$_5$ films and (D) P3HT$_{85}$-*g*-PCL$_{15}$ films upon different ON–OFF irradiation cycles using a LED (λ = 467 nm) at different increasing power intensities (67, 131, 205, and 255 mW cm^{-2}). The photocurrent density has been normalized by the thickness of the films before and after the exposure to thermo-oxidative conditions. (E) Schematic representation of the set-up used for measuring the H_2O_2 production. (F) Average values (3 replicates) of the H_2O_2 produced by the P3HT$_{95}$-*g*-PCL$_5$ and P3HT$_{85}$-*g*-PCL$_{15}$ films at the end of each illumination step, lasting 180 s, irradiated with a LED (λ = 467 nm; 67, 131, 205, and 255 mW cm^{-2}).

ponding pristine ones; however, there was no significant difference, especially at higher light intensities. Instead, for P3HT$_{85}$-*g*-PCL$_{15}$, we recorded a significant difference between the H_2O_2 produced by the porous film *vs.* the pristine one. Additionally, the amount of H_2O_2 produced was higher than that for P3HT$_{85}$-*g*-PCL$_{15}$ for the porous films. Although the AFM did not show the presence of big pores in the P3HT$_{85}$-*g*-PCL$_{15}$ copolymer, the results could be explained by the more homogeneous and macro-structured surface of the P3HT$_{85}$-*g*-PCL$_{15}$ *vs.* P3HT$_{95}$-*g*-PCL$_5$ films. The former had a macrostructure, while the latter was rather flat at the macroscale, hence the P3HT$_{85}$-*g*-PCL$_{15}$ films possibly exhibited a higher surface area, corresponding to a higher contact with the electrolyte, which allowed for a higher number of reaction sites. Overall, these results demonstrated the capability of nanostructured P3HT$_{95}$-*g*-PCL$_5$ films and P3HT$_{85}$-*g*-PCL$_{15}$ ones to modulate the ROS (*i.e.*, H_2O_2) production in the non-cytotoxic range for future redox medicine therapies.

3. Materials and methods

3.1 Materials

3-Hexylthiophene ≥98.0% (3HT) and hydroxymethyl EDOT ≥97.0% were supplied by TCI, and iron(III) chloride, methanol ≥99.9%, and chloroform ≥99.8% were purchased from Fluka. Methanesulfonic acid ≥99.0% (MSA), 4-(dimethylamino)pyridine ≥98.0% (DMAP), ε-caprolactone (CL), tetrahydrofuran (THF), and phosphate buffered saline (PBS) were purchased from Sigma-Aldrich.

3.2 Synthesis of PCL macromonomers

The α-EDOT-PCL macromonomer with a molecular weight of 9760 g mol^{-1} was synthesized by the ROP of ε-caprolactone in bulk using hydroxymethyl EDOT as a chain initiator and a mixture of MSA and DMAP (1MSA/1DMAP) as an organocatalyst. First, the organocatalyst mixture was heated up at 100 °C until a white salt formed. Then, ε-caprolactone and hydroxymethyl EDOT were added and left to react at 90 °C under magnetic stirring in an inert atmosphere for 5 days until a 90% conversion was achieved. The resulting product, EDOT-PCL, was purified through precipitation in methanol and vacuum-dried at room temperature overnight.

3.3 Synthesis of P3HT and P3HT-*g*-PCL copolymers

P3HT was synthesized by chemical oxidative copolymerization of 3HT using $FeCl_3$ as an oxidizing agent (4 equiv. of the respective 3HT monomer) and acetonitrile as a solvent at room temperature overnight, as reported previously.[22] Graft copolymers with different compositions were synthesized by the

chemical oxidative copolymerization of 3HT and the α-EDOT-PCL macromonomer using $FeCl_3$ (4 equiv. of the respective 3HT monomer) as an oxidizing agent and acetonitrile as a solvent. The reaction was carried out under magnetic stirring at room temperature overnight. In all cases, the dark brown dispersions obtained were precipitated in methanol, rinsed with methanol and water until the iron residue was fully removed, and dried under vacuum.

3.4 Proton nuclear magnetic resonance spectroscopy (^{1}H NMR)

^{1}H NMR spectra were recorded by using a Bruker ADVANCE DPX 300 at 300.16 MHz resonance frequency and room temperature, and by using $CDCl_3$ as the solvent. The experimental conditions were: 10 mg of the sample, 3 s acquisition time, 1 s delay time, 8.5 μs pulse, a spectral width of 5000 Hz, and 32 scans.

3.5 Film preparation

Films were prepared by drop casting on the ITO-glass substrates (3.7 × 4 mm, Ossila). First, non-porous films were prepared by dropping 20 μL of P3HT or P3HT-*g*-PCL solutions at a concentration of 20 mg mL^{-1} in a mixture of chlorobenzene and chloroform (50 : 50%v/v) over the ITO-glass substrate and letting it dry in a fume hood at 20 °C with an air recirculation flow rate of 0.39 m^3 s^{-1} for 12 h. Then, porous films were obtained in a second step by oxidation in the presence of 100 mM H_2O_2 at 42 °C for 48 h, followed by a rinsing step with water, and finally dried at room temperature.

3.6 Atomic force microscopy (AFM)

The morphology of the films was analyzed by AFM using a Bruker Multimode 8, with a Nanoscope V controller. All measurements were performed in the tapping mode, in air at room temperature. The analysis of the AFM images to calculate the roughness and the pore size (2 μm × 2 μm) was carried out using Nanoscope Analysis 1.90 software (Bruker).

3.7 Nanomechanical properties

Mechanical properties were assessed by nanoindentation. Samples were glued onto a metal holder, which was placed on the platform of a G200 nanoindenter equipped with a low load resolution head (KLA Tencor, Milpitas, California, USA) and a diamond indenter with Berkovich geometry. A small oscillating force (1 nm displacement amplitude, 75 Hz frequency) was superimposed on the quasi-static load. The phase lag between the harmonic force and the displacement allowed continuous calculation of the dynamic contact stiffness during the loading cycle (Continuous Stiffness Measurements, CSMs). During loading, the indentation strain rate was kept constant at 0.05 s^{-1}. The storage modulus (E') and hardness (H) were determined as a function of the indenter penetration depth (h) using the harmonic contact stiffness, with average values calculated from a minimum of 25 indentations. Poisson's ratio was assumed to be 0.4 in all cases and the indenter area function was calibrated using a fused silica standard.

3.8 Electrochemical characterization

The electrochemical characterization of the films was carried out in a three-electrode electrochemical cell, with PBS as the electrolyte, a platinum bundle as the Counter Electrode (CE), and Ag/AgCl (Sat) as the Reference Electrode (RE). A VMP3 BioLogic potentiostat was employed for electrochemical recording. The cell was kept in a Faraday cage to reduce electrical noise.

3.8.1 Photocurrent. Square $P3HT_{95}$-*g*-PCL_5 and $P3HT_{85}$-*g*-PCL_{15} films built on ITO-glass substrates (3.7 × 4 mm, Ossila) were immersed in PBS. A Kessil (PR160L) lamp with 467 nm central wavelength was employed for the photostimulation, with four intensity steps corresponding to 67, 131, 205, and 255 mW cm^{-2}. The illumination was carried out from the polymer side. The photocurrent was recorded at an open circuit voltage.

3.8.2 H_2O_2 production. For the H_2O_2 recording, black platinum electrodes were prepared according to the reported procedures,[38–40] to increase the sensitivity towards hydrogen peroxide. Briefly, black platinum was electrodeposited on platinum wires (300 μm diameter) in a three-electrode electrochemical cell, with a Pt bundle as the CE and an Ag/AgCl saturated KCl as the RE, in a 31.2 mM solution of hexachloroplatinic acid in PBS as the electrolyte. The electrodes were all characterized first by cyclic voltammetry in a freshly prepared 10 mM solution of H_2O_2 in PBS, identifying reduction and oxidation peaks. Then, the electrodes were washed and calibrated in a fresh PBS solution, in the range of 0–450 μM H_2O_2, keeping the WE at the H_2O_2 oxidation potential. After calibration, the H_2O_2 production from the $P3HT_{95}$-*g*-PCL_5 and $P3HT_{85}$-*g*-PCL_{15} films was evaluated. The film was placed at the bottom of a Petri dish, and the CE (Pt bundle) and RE (Ag/AgCl saturated KCl) were placed on the sides; the electrolyte was fresh PBS. The black platinum WE was placed on top of the film with a micromanipulator. The illumination was carried out with the same Kessil lamp (467 nm central wavelength) as used for the photocurrent characterization. We employed the same four light intensities (67, 131, 205, and 255 mW cm^{-2}) as for the photocurrent recording, for 180 s. The electrode was kept at the oxidation potential, and the current was converted to the concentration through the calibration curve previously mentioned. In between each experiment, the electrodes were thoroughly washed and fresh PBS was added for each condition.

Conclusions

Nanostructured photoactive films were obtained through the design and synthesis of graft copolymers made of a semiconducting polymer, P3HT, and a biocompatible and biodegradable polyester, PCL. The graft copolymers P3HT-*g*-PCL were successfully processed in the form of compact films by drop casting. After a thermo-oxidative treatment in the presence of H_2O_2 and at 42 °C, $P3HT_{95}$-*g*-PCL_5 films showed a nanostructured morphology with the presence of nanopores

(~500 nm diameter and ~70 nm height), while $P3HT_{85}$-*g*-PCL_{15} only showed a change in the surface roughness. In both cases, the changes in either the nano- or the microstructure influenced the production of ROS positively when irradiated with a visible light LED (467 nm), which led to a controlled increase of H_2O_2 in the non-cytotoxic range. It would be useful to be used as patches for potential minimally invasive redox medicine therapies. This understanding of photoinduced ROS generation is of paramount importance for the potential treatment of many diseases, such as cardiovascular pathologies and cancer, which are closely connected to the modulation of intracellular ROS concentration. Additionally, this approach potentially enables the use of inflammation-responsive functional materials.

Author contributions

I. A. A.: experimental research, formal analysis, and writing. E. G.: experimental research synthesis macromonomers and formal analysis. A. F.: nanomechanical properties and formal analysis. P. P.: AFM measurements. H. S.: supervision and funding acquisition. D. M.: conceptualization, supervision, funding acquisition, and writing. M. C.-G.: conceptualization, experimental research, formal analysis, supervision, funding acquisition, writing, review, and editing.

Data availability

The data supporting this article have been included as part of the ESI.†

Conflicts of interest

There are no conflicts to declare.

Acknowledgements

The authors acknowledge the grants PID2020-119026GB-I00 and PID2020-117573GB-I00 funded by MCIN/AEI/10.13039/501100011033. M. C.-G. thanks "Ayuda RYC2022-036380-I financiada por MICIU/AEI /10.13039/501100011033 y por el FSE+" and the Emakiker program of POLYMAT (UPV/EHU). This work was funded by the European Union's Horizon 2020 research and innovation programme under the Marie Sklodowska-Curie grant agreement no. 101034379.

References

1 M. P. Murphy, H. Bayir, V. Belousov, C. J. Chang, K. J. A. Davies, M. J. Davies, T. P. Dick, T. Finkel, H. J. Forman, Y. Janssen-Heininger, D. Gems, V. E. Kagan, B. Kalyanaraman, N.-G. Larsson, G. L. Milne, T. Nyström, H. E. Poulsen, R. Radi, H. Van Remmen, P. T. Schumacker, P. J. Thornalley, S. Toyokuni, C. C. Winterbourn, H. Yin and B. Halliwell, *Nat. Metab.*, 2022, **4**, 651–662.
2 M. Criado-Gonzalez and D. Mecerreyes, *J. Mater. Chem. B*, 2022, **10**, 7206–7221.
3 H. Sies, *J. Biol. Chem.*, 2014, **289**, 8735–8741.
4 M. Regato-Herbella, D. Mantione, A. Blachman, A. Gallastegui, G. C. Calabrese, S. E. Moya, D. Mecerreyes and M. Criado-Gonzalez, *ACS Macro Lett.*, 2024, **13**, 1119–1126.
5 H. Sies and D. P. Jones, *Nat. Rev. Mol. Cell Biol.*, 2020, **21**, 363–383.
6 J. D. West and L. J. Marnett, *Chem. Res. Toxicol.*, 2006, **19**, 173–194.
7 L. Zhang, X. Wang, R. Cueto, C. Effi, Y. Zhang, H. Tan, X. Qin, Y. Ji, X. Yang and H. Wang, *Redox Biol.*, 2019, **26**, 101284.
8 A. Kaur, J. L. Kolanowski and E. J. New, *Angew. Chem., Int. Ed.*, 2016, **55**, 1602–1613.
9 S. George, M. R. Hamblin and H. Abrahamse, *J. Photochem. Photobiol., B*, 2018, **188**, 60–68.
10 L. Sun, C. Cheng, S. Wang, J. Tang, R. Xie and D. Wang, *ACS Nano*, 2021, **15**, 12475–12482.
11 F. Lodola, N. Martino, G. Tullii, G. Lanzani and M. R. Antognazza, *Sci. Rep.*, 2017, **7**, 8477.
12 M. R. Antognazza, I. Abdel Aziz and F. Lodola, *Oxid. Med. Cell. Longevity*, 2019, **2019**, 2867516.
13 Y. Yu, H. Y. Y. Nyein, W. Gao and A. Javey, *Adv. Mater.*, 2020, **32**, 1902083.
14 D. Gao, K. Parida and P. S. Lee, *Adv. Funct. Mater.*, 2020, **30**, 1907184.
15 D. Ghezzi, M. R. Antognazza, R. Maccarone, S. Bellani, E. Lanzarini, N. Martino, M. Mete, G. Pertile, S. Bisti, G. Lanzani and F. Benfenati, *Nat. Photonics*, 2013, **7**, 400–406.
16 D. Ghezzi, M. R. Antognazza, M. Dal Maschio, E. Lanzarini, F. Benfenati and G. Lanzani, *Nat. Commun.*, 2011, **2**, 166.
17 I. Abdel Aziz, M. Malferrari, F. Roggiani, G. Tullii, S. Rapino and M. R. Antognazza, *iScience*, 2020, **23**, 101091.
18 L. Bondi, C. Marzuoli, E. Gutiérrez-Fernández, G. Tullii, J. Martín, B. Fraboni, D. Mecerreyes, M. R. Antognazza and T. Cramer, *Adv. Electron. Mater.*, 2023, **9**, 2300146.
19 J. F. Maya-Vetencourt, G. Manfredi, M. Mete, E. Colombo, M. Bramini, S. Di Marco, D. Shmal, G. Mantero, M. Dipalo, A. Rocchi, M. L. DiFrancesco, E. D. Papaleo, A. Russo, J. Barsotti, C. Eleftheriou, F. Di Maria, V. Cossu, F. Piazza, L. Emionite, F. Ticconi, C. Marini, G. Sambuceti, G. Pertile, G. Lanzani and F. Benfenati, *Nat. Nanotechnol.*, 2020, **15**, 698–708.
20 M. Criado-Gonzalez, C. Marzuoli, L. Bondi, E. Gutierrez-Fernandez, G. Tullii, P. Lagonegro, O. Sanz, T. Cramer, M. R. Antognazza and D. Mecerreyes, *Nano Lett.*, 2024, **24**, 7244–7251.
21 C. Tortiglione, M. R. Antognazza, A. Tino, C. Bossio, V. Marchesano, A. Bauduin, M. Zangoli, S. V. Morata and G. Lanzani, *Sci. Adv.*, 2017, **3**, e1601699.

22 M. Criado-Gonzalez, L. Bondi, C. Marzuoli, E. Gutierrez-Fernandez, G. Tullii, C. Ronchi, E. Gabirondo, H. Sardon, S. Rapino, M. Malferrari, T. Cramer, M. R. Antognazza and D. Mecerreyes, *ACS Appl. Mater. Interfaces*, 2023, **15**, 35973–35985.
23 I. Abdel Aziz, L. Maver, C. Giannasi, S. Niada, A. T. Brini and M. R. Antognazza, *J. Mater. Chem. C*, 2022, **10**, 9823–9833.
24 A. Dominguez-Alfaro, M. Criado-Gonzalez, E. Gabirondo, H. Lasa-Fernández, J. L. Olmedo-Martínez, N. Casado, N. Alegret, A. J. Müller, H. Sardon, A. Vallejo-Illarramendi and D. Mecerreyes, *Polym. Chem.*, 2022, **13**, 109–120.
25 M. J. Leite, T. Agner, F. Machado, B. A. D. Neto, P. H. H. Araujo and C. Sayer, *J. Polym. Res.*, 2022, **29**, 56.
26 D. S. Dissanayake, E. Sheina, M. C. Biewer, R. D. McCullough and M. C. Stefan, *J. Polym. Sci., Part A: Polym. Chem.*, 2017, **55**, 79–82.
27 S. Marina, D. Mantione, K. ManojKumar, V. Kari, J. Gutierrez, A. Tercjak, A. Sanchez-Sanchez and D. Mecerreyes, *Polym. Chem.*, 2018, **9**, 3780–3790.
28 R. Dattani, J. H. Bannock, Z. Fei, R. C. I. MacKenzie, A. A. Y. Guilbert, M. S. Vezie, J. Nelson, J. C. de Mello, M. Heeney, J. T. Cabral and A. J. Nedoma, *J. Mater. Chem. A*, 2014, **2**, 14711–14719.
29 P.-H. Hsu, C. Arboleda, A. Stubelius, L.-W. Li, J. Olejniczak and A. Almutairi, *Biomater. Sci.*, 2020, **8**, 2394–2397.
30 A. Elschner, S. Kirchmeyer, W. Lovenich, U. Merker and K. Reuter, *PEDOT Principles and Applications of an Intrinsically Conductive Polymer*, CRC Press, Boca Raton, 1st edn, 2010.
31 M. Manceau, A. Rivaton, J.-L. Gardette, S. Guillerez and N. Lemaître, *Polym. Degrad. Stab.*, 2009, **94**, 898–907.
32 H. Ohta and H. Koizumi, *Polym. Bull.*, 2017, **74**, 2319–2330.
33 L. Kong, G. Li and X. Wang, *Catal. Today*, 2004, **93–95**, 341–345.
34 S. Heedy, J. J. Pineda, V. S. Meli, S.-W. Wang and A. F. Yee, *ACS Nano*, 2022, **16**, 3311–3322.
35 Á. M. López, J. Berglund, K. Marteleur and A. Finne-Wistrand, *Bioprinting*, 2023, **33**, e00293.
36 J. K. Palacios, R. M. Michell and A. J. Müller, *Polym. Test.*, 2023, **121**, 107995.
37 B. Ilic, D. Czaplewski, P. Neuzil, T. Stanczyk, J. Blough and G. J. Maclay, *J. Mater. Sci.*, 2000, **35**, 3447–3457.
38 S. Ben-Amor, E. Vanhove, F. Sékli Belaïdi, S. Charlot, D. Colin, M. Rigoulet, A. Devin, N. Sojic, J. Launay, P. Temple-Boyer and S. Arbault, *Electrochim. Acta*, 2014, **126**, 171–178.
39 S. E. Stanca, F. Hänschke, A. Ihring, G. Zieger, J. Dellith, E. Kessler and H. G. Meyer, *Sci. Rep.*, 2017, **7**, 1074.
40 S.-E. Stanca, O. Vogt, G. Zieger, A. Ihring, J. Dellith, A. Undisz, M. Rettenmayr and H. Schmidt, *Commun. Chem.*, 2021, **4**, 98.